

# Te nanomesh/black-Si van der Waals Heterostructure for High-Performance Photodetector

Yiyang Wei, Changyong Lan,\* Ji Zeng, You Meng, Shuren Zhou, SenPo Yip, Chun Li, Yi Yin, and Johnny C. Ho

Van der Waals (vdW) heterostructures have gained significant attention in photodetectors due to their seamless integration with materials possessing diverse functionalities. In this study, the fabrication of a Te nanomesh/black-Si vdW heterostructure is presented, and investigated its photoresponse properties. The heterostructure exhibits a pronounced rectification behavior, characterized by a rectification ratio of  $2.2 \times 10^4$ . Notably, the heterostructure device demonstrates commendable photoresponse properties, including a high responsivity of  $350 \text{ mA W}^{-1}$ , an extensive linear dynamic range of 45.5 dB, a high specific detectivity of  $9.6 \times 10^{11}$  Jones, and a wide spectral response ranging from 400 to 1550 nm. Furthermore, the heterostructure exhibits rapid response, with a rise time and a decay time of 70 and 140  $\mu\text{s}$ , respectively. These exceptional photoresponse properties can be attributed to the robust internal built-in electrical field at the hetero-interface and the augmented light absorption in black-Si. The outstanding photoresponse properties of the heterostructure make it a promising candidate for multiwavelength single-pixel imaging, enabling the collection of mask patterns under varying wavelengths of light radiation. This work provides a novel approach for fabricating mixed-dimensional vdW heterostructures, offering promising prospects for advancements in optoelectronics.

## 1. Introduction

Photodetectors play a vital role in modern society, finding applications in various fields, including optical communications,<sup>[1]</sup> spectral analysis,<sup>[2]</sup> remote sensing,<sup>[3]</sup> autopilot, and full self-driving

capability.<sup>[4]</sup> Among the diverse range of photodetectors available, Si-based photodetectors are the most commonly used due to their well-established fabrication techniques, decent photodetection performance, and cost-effectiveness. Due to the band gap constraint, Si photodetectors inevitably face limitations in detecting light with wavelengths longer than 1100 nm. In this regard, to overcome this limitation, alternative photodetector technologies have been widely studied, such as those based on InGaAs, superlattices, HgCdTe, and quantum dots, which are capable of detecting light in the infrared regime.<sup>[5–8]</sup> However, these photodetectors often require complex fabrication techniques and are associated with high costs.<sup>[8]</sup> In light of these challenges, there is a pressing need to explore new materials that can enable the development of broadband photodetectors.

In recent years, there has been significant interest in van der Waals (vdW) materials because of their unique properties.<sup>[9–18]</sup> Various vdW materials with diverse properties have been discovered, including narrow

band gap materials like black phosphorus, PdSe<sub>2</sub>, and Te. These materials hold great promise for infrared photodetection.<sup>[11,19–21]</sup> For instance, Yu et al. demonstrated that a photodetector based on bilayer PtSe<sub>2</sub> exhibited an ultrabroad band photoresponse, spanning from visible to mid-infrared light (10.0  $\mu\text{m}$ ).<sup>[22]</sup> One of the advantages of vdW materials is their ability to be easily integrated with other materials without concerns about lattice mismatch, thanks to the presence of dangling-free surfaces. Researchers have successfully integrated narrow band gap vdW materials with Si, forming heterostructure photodetectors that exhibit superior performance across a wide spectral range.<sup>[23]</sup> For example, Lu et al. fabricated few-layer MoTe<sub>2</sub>/Si heterojunction photodiodes with a remarkable spectral response ranging from 300 to 1800 nm.<sup>[24]</sup> Researchers have incorporated black-Si into vdW heterostructures to enhance the light absorption capability, as flat-Si has weak light absorption.<sup>[25–27]</sup> This integration has shown significant improvements in the performance of heterostructure photodetectors. Particularly, Liang et al. successfully fabricated a multilayer PdSe<sub>2</sub>/pyramid Si heterojunction and observed excellent photoresponse properties, including a large current on/off ratio of  $1.6 \times 10^5$  and a high responsivity of  $456 \text{ mA W}^{-1}$ .<sup>[25]</sup> Therefore, the integration of vdW materials with

Y. Wei, C. Lan, J. Zeng, S. Zhou, C. Li, Y. Yin  
State Key Laboratory of Electronic Thin Film and Integrated Devices,  
School of Optoelectronic Science and Technology  
University of Electronic Science and Technology of China  
Chengdu 611731, China  
E-mail: [cylan@uestc.edu.cn](mailto:cylan@uestc.edu.cn)

Y. Meng, J. C. Ho  
School of Materials Science and Engineering  
City University of Hong Kong  
Hong Kong 999077, China

S. Yip, J. C. Ho  
Institute for Materials Chemistry and Engineering  
Kyushu University  
Fukuoka 816 8580, Japan

The ORCID identification number(s) for the author(s) of this article can be found under <https://doi.org/10.1002/adom.202400056>

DOI: 10.1002/adom.202400056

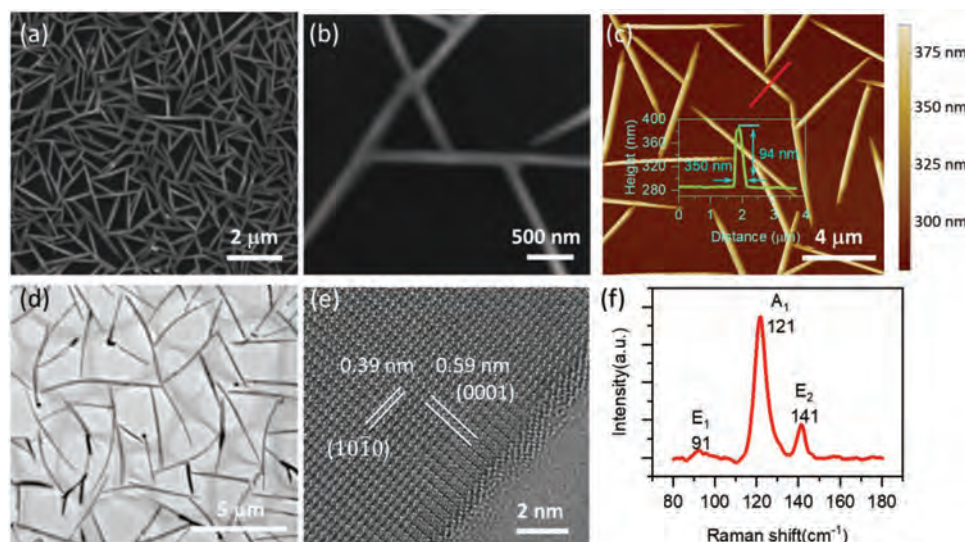


**Figure 1.** Characterization of the Te nanomesh. a) Low-magnification SEM image. b) High-magnification SEM image. c) AFM image. Inset: Height profile along the red line. d) TEM image of the Te nanomesh. e) HRTEM image of the Te nanowires. f) Raman spectrum.

Si in heterostructure configurations holds tremendous promise for the development of high-performance photodetectors.

At the same time, among many vdW candidates, Te is a quasi-1D vdW material with remarkable electronic and optoelectronic properties, including high carrier mobility, a narrow band gap, and high environmental stability.<sup>[28,29]</sup> Amani et al. demonstrated that photodetectors based on solution-synthesized Te nanoflakes exhibited a broadband spectral response from visible light to 3.5  $\mu\text{m}$  and high responsivity.<sup>[30]</sup> Similarly, Peng et al. found that photodetectors based on chemical vapor deposition-synthesized Te nanowires and nanosheets showed a broad spectral response and high sensitivity to blackbody radiation.<sup>[31]</sup> Given the narrow band gap of Te (0.35 eV),<sup>[32]</sup> the Te/Si heterostructure photodetector is expected to yield a desirable broadband response. In addition, it is worth noting that there has been limited research conducted thus far on the exploration of nanomesh/Si heterostructures, which hold great potential for delivering novel optoelectronic properties.

Recently, we reported the synthesis of Te nanomesh with promising properties through low-temperature physical vapor deposition.<sup>[33]</sup> The low-temperature synthesis method is compatible with complementary metal-oxide-semiconductor processes and enables the direct growth of Te nanomesh on various substrates, including Si. This direct growth approach ensures a high-quality interface between Te nanomesh and Si, which is advantageous for photodetection performance. Leveraging the enhanced light absorption capabilities of black-Si, the Te nanomesh/black-Si heterostructure is anticipated to give favorable photoresponse properties. In this work, we successfully fabricated a Te nanomesh/black-Si heterostructure by directly growing Te nanomesh on the surface of black-Si. The heterostructure exhibited typical rectification behavior with a high rectification ratio of  $2.2 \times 10^4$ . Furthermore, the heterojunction photodetector demonstrated commendable photoresponse performance, including a high responsivity of  $350 \text{ mA W}^{-1}$ , a large linear dynamic range of 45.5 dB, a high specific detectivity of  $9.6 \times 10^{11}$

Jones, fast response speeds, and a wide spectral response from visible light to 1550 nm. Moreover, the photodetector exhibited self-power capability with stable responses. As a demonstration, we showcased the functionality of the heterostructure as a single-pixel imager capable of detecting images across a broad spectrum of wavelengths. Our work provides a straightforward method for fabricating mixed-dimensional vdW heterostructures with promising performance, paving the way for their applications in next-generation optoelectronics.

## 2. Results and Discussion

The scanning electron microscopy (SEM) image of the Te nanomesh is shown in **Figure 1a**. The Te nanowires are interconnected, forming a Te nanomesh. These Te nanowires have lengths in the range of several micrometers. **Figure 1b** presents a high magnification SEM image of the Te nanomesh, which was used to determine the average diameter of the Te nanowires, measuring  $\approx 130 \text{ nm}$ . The distribution of the Te nanowire diameter is depicted in **Figure S1** (Supporting Information), revealing a mean diameter of 135 nm. Atomic force microscopy (AFM) images were utilized to characterize the morphology of the Te nanomesh further. **Figure 1c** displays a representative AFM image of the Te nanomesh, exhibiting a similar morphology to that observed in the SEM image. The height profile along the red line in the figure is shown in the inset of **Figure 1c**, revealing a height of 90 nm and a width of 350 nm. Notably, the large width from the AFM test does not accurately represent the true width of the Te nanowire due to the smearing effect caused by the AFM tip. Nonetheless, the AFM image illustrates a mesh structure consistent with the SEM findings. The low magnification transmission electron microscopy (TEM) image displayed in **Figure 1d** showcases the nanomesh structure, with the observed low density of nanowires attributed to the loss of some during the sample preparation process. A high-resolution TEM (HRTEM) image of a nanowire was recorded and presented in **Figure 1e** to assess

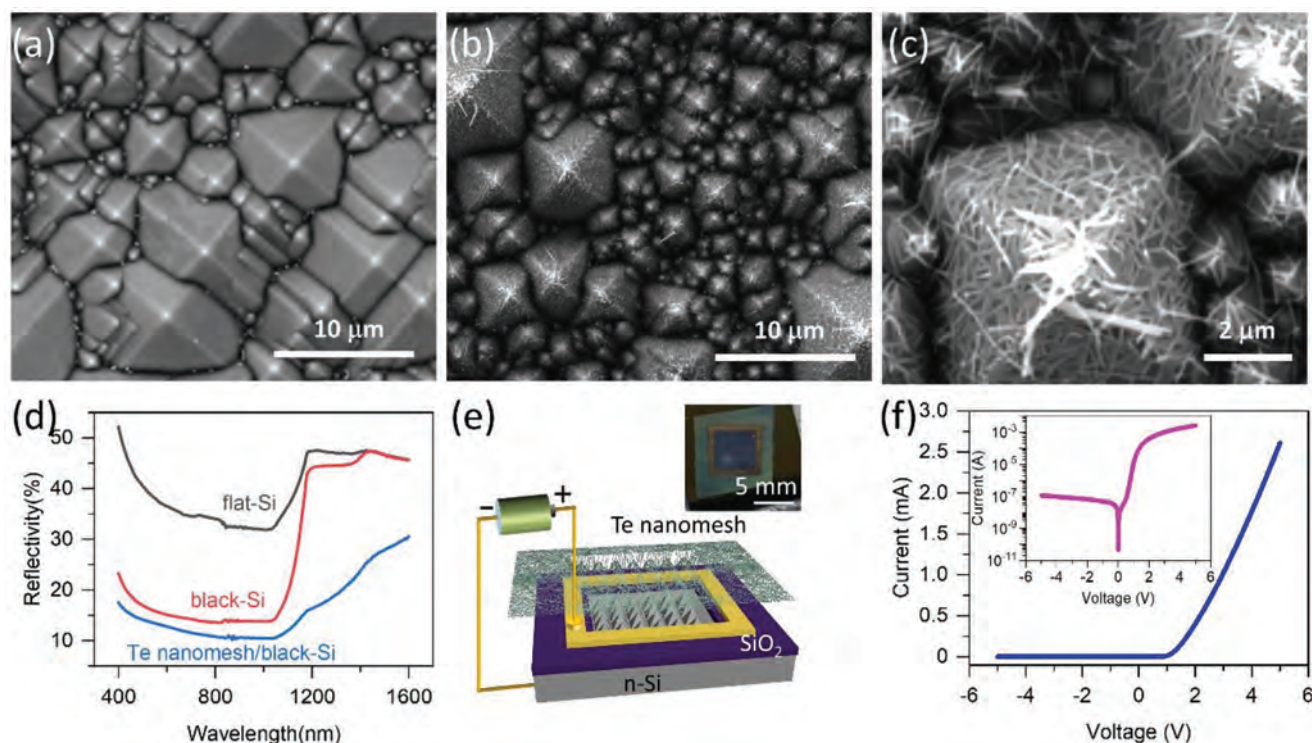


**Figure 2.** Characterization of the Te nanomesh/black-Si heterostructure and its electrical properties. a) SEM image of black-Si. b) SEM image of Te nanomesh/black-Si. c) high-magnification SEM image of the Te nanomesh/black-Si. d) Reflectance spectra of flat-Si, black-Si, and Te nanomesh/black-Si. e) Schematic of the Te nanomesh/black-Si heterostructure device. The inset shows the digital photograph of the device. f) Current-voltage curve. The inset gives the semi-log plot of the current-voltage curve.

the crystallinity of the Te nanowires. Clear lattice fringes are observed, indicating the good crystallinity of the Te nanowires. The lattice spacings were evaluated and found to be 0.39 and 0.59 nm, corresponding to (10 $\bar{1}$ 0) and (0001) planes of Te, respectively. Additionally, the Raman spectrum of the Te nanomesh was measured and is presented in Figure 1f. Peaks located at 91, 121, and 141 cm $^{-1}$  are observed, corresponding to the E $_1$ , A $_1$ , and E $_2$  modes of Te, respectively.<sup>[30]</sup>

The black-Si window was fabricated using a combination of the wet-etching method and the photolithography technique. Figure 2a shows the surface morphology of the black-Si, revealing the presence of micrometer-scale pyramids. After the physical vapor deposition process, a layer of Te nanomesh was coated onto the pyramids, as shown in Figure 2b. Figure 2c presents a high-magnification SEM image of the Te nanomesh/black-Si heterostructure, demonstrating the close alignment between the Te nanomesh and the Si pyramids. Moreover, the Te nanowires are densely distributed on the lateral surfaces of the pyramids but are less abundant at the pyramid roots. It is noteworthy to mention that the Te nanowires interconnect, forming a continuous Te nanomesh capping layer. Typically, black-Si exhibits higher light absorption than flat-Si due to the light-trapping effect. To verify the enhanced light absorption of black-Si, reflectance spectra were measured for both flat-Si and black-Si, as shown in Figure 2d. The results indicate that black-Si displays significantly reduced light reflectance across a wide spectral range, ranging from ultraviolet to near-infrared, compared with flat-Si, confirming the enhanced light absorption of black-Si. Further-

more, the reflectance further decreases after the capping with Te nanomesh, suggesting additional light absorption by the Te nanomesh. The improved light absorption is beneficial for enhancing the photodetection performance of the heterostructure. Consequently, a photodetector based on the heterostructure was fabricated, as schematically illustrated in Figure 2e. A digital photograph of the heterostructure device is shown in the inset of Figure 2e. The Te nanomesh exhibits p-type conductivity, as reported in our previous paper,<sup>[33]</sup> while n-doped Si was utilized in this study. Thus, a pn heterojunction is formed between the Te nanomesh and black-Si. Before investigating the device's photoresponse properties, the electrical behavior in the dark state was initially examined, and the resulting current-voltage curve is presented in Figure 2f. The n-Si was grounded during the measurement, and the electrode connected to the Te nanomesh served as the drain. The device exhibits distinctive rectification behavior, with minimal current observed under reverse bias and significant current flow under forward bias. As illustrated in Figure S2 (Supporting Information), the Ti/Au electrode and Ag paste establish Ohm-like contact with Te nanomesh and n-Si, respectively, indicating that the rectification originates from the Te/Si heterostructure. A semilog plot of the current-voltage curve is included as an inset in Figure 2f to illustrate the rectification behavior. The forward current is orders of magnitude higher than the reverse current, resulting in a rectification ratio of  $\approx 2.2 \times 10^4$  at  $\pm 5$  V, indicating favorable diode characteristics. The current-voltage relationship of diodes can be described by the equation:  $I_{ds} = I_s [\exp(qV_{ds}/nkT) - 1]$ , where  $I_s$  is the reverse saturated



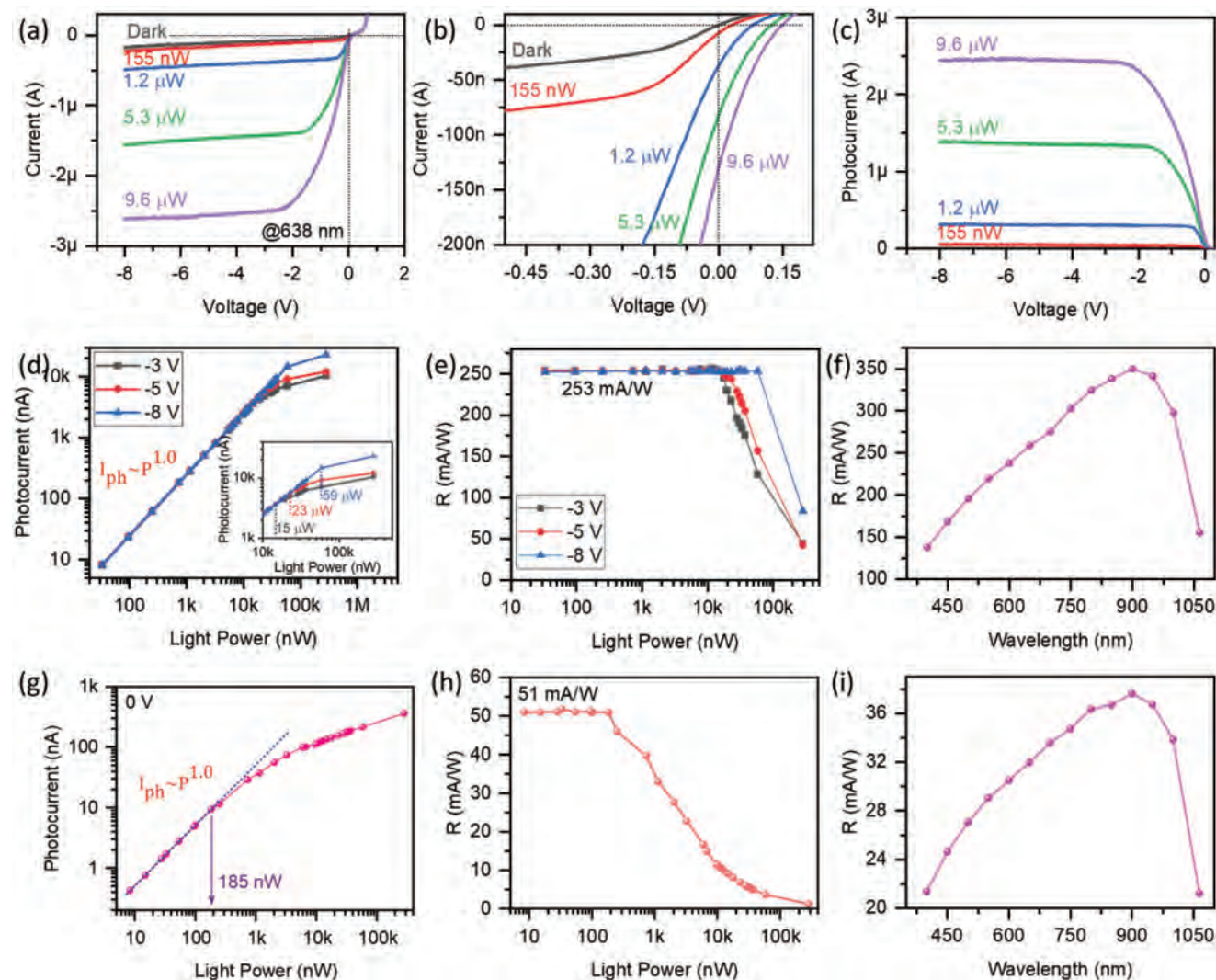


**Figure 3.** Photoresponse properties of the Te nanomesh/black-Si heterostructure. a) Current–voltage curves under light radiation at various powers and in the dark state. b) Magnified section near zero bias. c) Photocurrent–voltage curves under light radiation at different powers. d) Photocurrent as a function of light power at different bias voltages. e) Responsivity as a function of light power at different bias voltages. f) Spectral response at a bias voltage of  $-5$  V and a light power of  $3$   $\mu$ W. g) Photocurrent as a function of light power with zero bias voltage. h) Responsivity as a function of light power with zero bias voltage. i) Spectral response at zero bias voltage and with a light power of  $3$   $\mu$ W. The wavelength of light for (a–e) and (g–h) is  $638$  nm.

current,  $q$  is the elementary charge value,  $n$  is the ideality factor,  $k$  is the Boltzmann constant, and  $T$  is the temperature in Kelvin. Accordingly, the ideality factor of the device was determined to be  $3.5$ , as shown in Figure S3 (Supporting Information). The large ideality factor suggests that the forward current in the device is dominated by tunneling processes rather than diffusion or recombination processes.<sup>[34,35]</sup>

To shed light on the photoresponse properties of the Te nanomesh/black-Si heterostructure, the current–voltage curves were obtained under both light radiation ( $638$  nm) and no light radiation conditions, as shown in Figure 3a. It is evident that the absolute value of the current under reverse bias significantly increases upon light radiation, indicating a notable sensitivity to light. Moreover, the absolute value of the current rises with increasing light power. Figure 3b provides a magnified view of these curves, revealing that the detector exhibits photoresponse

even under zero bias, showcasing its self-powered capability. Photocurrent ( $I_{ph}$ ) is defined as the difference between the current in the light radiation state ( $I_{light}$ ) and the dark state ( $I_d$ ), represented as  $I_{ph} = |I_{light} - I_d|$ . Figure 3c presents the photocurrent as a function of reverse bias voltage. Initially, the photocurrent increases and eventually saturates with increasing reverse bias voltage. This saturation behavior aligns with conventional photodiodes, suggesting the absence of photo-gain in the detector. The critical reverse voltage leading to the photocurrent saturation depends on the incident light power, which increases with the light power. Measurements were conducted under different reverse bias voltages to investigate how the photocurrent varies with the incident light power, as shown in Figure 3d. At first, the photocurrent exhibits a linear increase with light power, transitioning to a sublinear relationship when the light power surpasses a critical value known as  $P_{sat}$ . The value of the critical light power depends

on the reverse bias voltage, as illustrated in the inset of Figure 3d. Specifically, the critical light power increases from 15 to 59  $\mu\text{W}$  as the absolute value of the reverse bias voltage increases from 3 to 8 V. Photoresponsivity, or simply responsivity ( $R$ ), is a critical parameter for evaluating the performance of a photodetector. It is expressed as:

$$R = \frac{I_{\text{ph}}}{P} \quad (1)$$

where  $P$  is the light power incident on the photosensitive area. Figure 3e illustrates the calculated responsivity as a function of light power. At low light powers, a constant responsivity of about 253  $\text{mA W}^{-1}$  is observed, consistent with the linear relationship witnessed in the photocurrent. However, when the light power surpasses the critical light power, the responsivity starts to decrease due to the sublinear behavior. The noise equivalent power ( $\text{NEP}$ ,  $P_{\text{NEP}}$ ) refers to the minimum detectable light power and holds significant importance in photodetectors. It is defined as the light power at which the photocurrent generated equals the root mean square current noise ( $i_n$ ). The NEP can be determined using the equation:

$$P_{\text{NEP}} = i_n / R \quad (2)$$

The root mean square noise current, i.e., noise current, can be obtained from the current–time curve in the dark state, as shown in Figure S4 (Supporting Information). It should be noted that the root mean square current noise depends on the bias voltage, which consequently affects the NEP. In this case, the NEPs are calculated to be 1.24, 1.38, and 1.68  $\text{nW}$  under the bias voltages of  $-3$ ,  $-5$ , and  $-8$  V, respectively, exhibiting a slight increase with reverse bias voltage. Typically, the NEP is normalized to the bandwidth of the measurement system. The normalized NEPs are  $9.35 \times 10^{-11}$ ,  $1.02 \times 10^{-10}$ , and  $1.27 \times 10^{-10} \text{ W}/\sqrt{\text{Hz}}$  under the bias voltages of  $-3$ ,  $-5$ , and  $-8$  V, respectively. Further details of the calculations can be found in the supporting information. Using the NEP value, the linear dynamic range (LDR,  $r$ ) of the photodetector can be determined from the following equation.

$$r = 10 \log \left( \frac{P_{\text{sat}}}{P_{\text{NEP}}} \right) \quad (3)$$

By applying this equation, the LDRs of the photodetector are found to be 40.8, 42.2, and 45.5 dB under the bias voltages of  $-3$ ,  $-5$ , and  $-8$  V, respectively. These values are comparable to those of some commercial Si photodiodes, such as the FDS100 from Thorlabs. Specific detectivity ( $D^*$ ) is another parameter used to characterize the capability of a photodetector, similar to NEP, in detecting weak light. However, specific detectivity is independent of the photosensitive area ( $A$ ) and bandwidth ( $B$ ), enabling comparison among different devices. Specific detectivity can be calculated using the following equation:

$$D^* = \frac{\sqrt{AB}}{P_{\text{NEP}}} \quad (4)$$

The specific detectivity values are calculated and shown in Figure S5 (Supporting Information). The specific detectivities are

$5.4 \times 10^9$ ,  $4.9 \times 10^9$ , and  $3.9 \times 10^9$  Jones under the bias voltages of  $-3$ ,  $-5$ , and  $-8$  V, respectively. Next, the spectral response of the heterostructure photodetector was measured at a bias voltage of  $-5$  V under constant light power mode ( $3 \mu\text{W}$ ), as displayed in Figure 3f. A peak responsivity of 350  $\text{mA W}^{-1}$  is observed at a wavelength of 900 nm. The spectral response profile closely resembles that of Si photodiodes, indicating that the main contribution to the photocurrent comes from the Si side. This effect can be attributed to both the Te nanomesh's hollow structure and the thin thickness.

The device's ability to operate at zero bias prompted the photocurrent measurement as a function of light power under zero bias, as shown in Figure 3g. The device exhibits a limited linear response range, with a sublinear response observed when the incident light intensity exceeds 185  $\text{nW}$ . In ideal diodes, a linear response is expected at zero bias. However, it is challenging to completely avoid unwanted charge traps in the heterojunction, resulting in a notable nonlinear response.<sup>[36,37]</sup> The corresponding responsivity, calculated as a function of light power, is presented in Figure 3h. Notably, the photoresponsivity at zero bias is significantly lower than that observed at a bias voltage of  $-5$  V, indicating a significant loss of photogenerated carriers at zero bias. The spectral response under zero bias is shown in Figure 3i. This profile closely resembles the spectral response observed under reverse bias, as shown in Figure 3f, indicating that the bias voltage does not alter the spectral response of the device. Furthermore, calculations were performed to determine the NEP, normalized NEP, and specific detectivity of the device under zero bias. The values obtained are 5.8  $\text{pW}$ ,  $5.23 \times 10^{-12} \text{ W}/\sqrt{\text{Hz}}$ , and  $9.6 \times 10^{11}$  Jones. For comparative purposes, the specific detectivity at zero bias is also included in Figure S5 (Supporting Information). The significantly enhanced specific detectivity achieved at zero bias can be attributed to the ultralow NEP observed at zero bias.

The dynamic response of the photodetector is crucial for practical applications, and we conducted measurements using a light wavelength of 638 nm. The current of the device demonstrates stable on-and-off switching behavior when the light is turned on and off, both at zero bias and with a bias voltage of  $-5$  V, as shown in Figure 4a,b, respectively. When subjected to an incident light power of 6.9  $\text{mW}$ , the device exhibits the current and on/off ratios of  $2.9 \times 10^4$  and 80, respectively. It is important to note that a high light-induced current on/off ratio at zero bias in a photodiode holds no significance despite its frequent mention in literature. The mean dark current at zero bias must be zero, as there is no energy to drive the formation of a positive or negative current. The dark current obtained from the semiconductor analyzer is attributed to zero drift. Additionally, the device demonstrated consistent performance even after being stored in the atmosphere for five months (Figure S6, Supporting Information), indicating its notable long-term stability. High-resolution current–time curves were measured by an oscillator to determine the response time of the device.<sup>[27]</sup> A typical current–time curve with a bias voltage of  $-5$  V is presented in Figure 4c. The rise time and decay time, defined as the time intervals for the current to rise from 10% to 90% of the static photocurrent and vice versa, respectively, were measured. The rise time and decay time, as observed in Figure 4c, are 70 and 140  $\mu\text{s}$ , respectively, indicating the fast response speed of the device. The

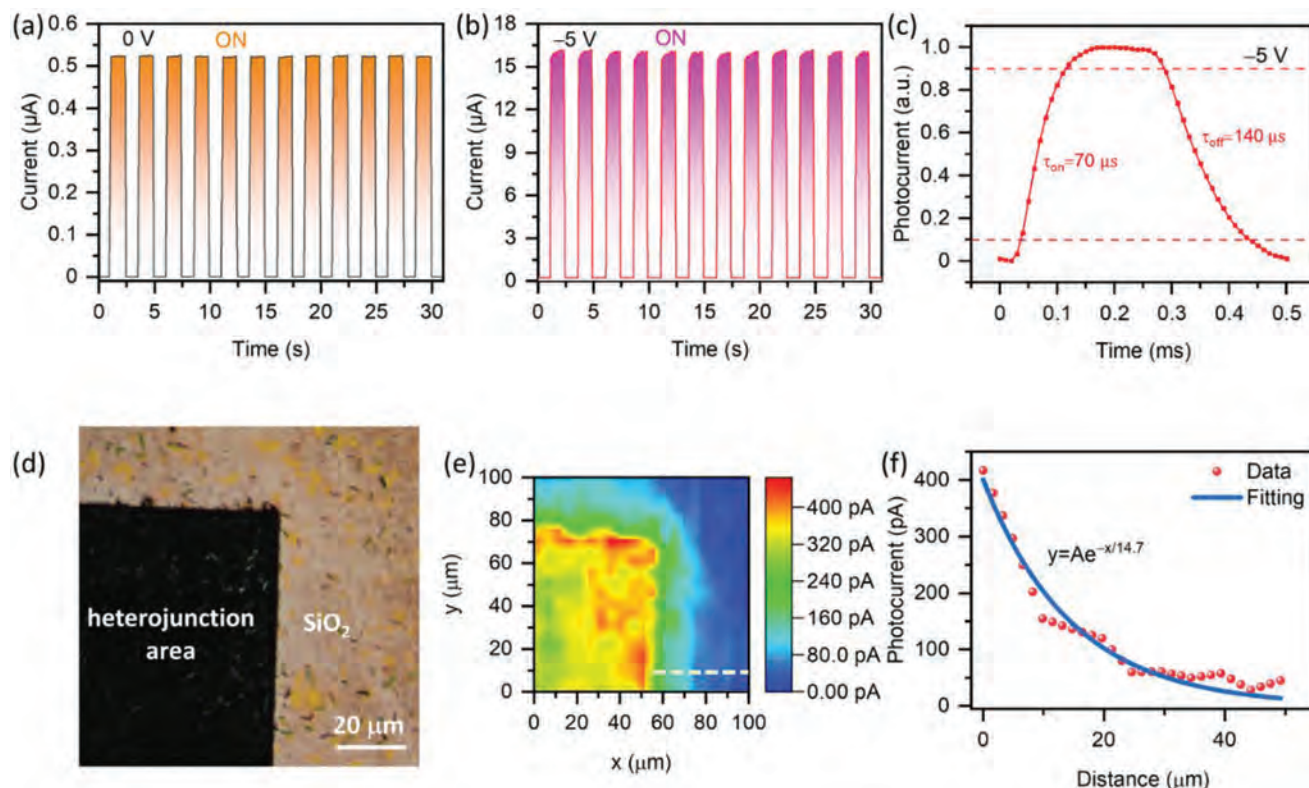


**Figure 4.** Dynamic response and photocurrent mapping (light wavelength: 638 nm). a) Current-time curves under modulated light at zero bias. b) Current-time curves under modulated light with a bias voltage of  $-5$  V. The light power radiated on the device for (a) and (b) is 6.9 mW. c) High-resolution current-time curve recorded by an oscillator. d) Digital photograph of the device. e) The corresponding photocurrent mapping at zero bias voltage. The light wavelength, spot size, and light power are 638 nm, 1.3  $\mu\text{m}$ , and 7 nW, respectively. f) Photocurrent along the white dashed line in (e).

fast response speed is attributed to the large internal electrical field at the heterojunction interface, while the variation between the rise time and decay time results from the intricate dynamics of the photogenerated carriers in the detector. For a better comparison of our device with those reported in the literature, Table 1 provides a summary of the photodetection performance of various heterostructures reported in previous studies. It can be observed that our device demonstrates a decent balance in terms of responsivity, detectivity, LDR, and response time.

To obtain a further understanding of the photosensitive device area, photocurrent mapping was conducted at zero bias. The measured area and the results are displayed in Figure 4d,e, respectively. As anticipated, the heterojunction region is proved to be the most light-sensitive area, displaying the highest photocurrent. A larger area photocurrent mapping is shown in Figure S7 (Supporting Information), revealing a non-uniform distribution of photocurrent. This non-uniform distribution of photocurrent in the heterojunction area is attributed to the

**Table 1.** Photodetection performance of heterostructure-based detectors.

Materials	$R/\text{mA}\cdot\text{W}^{-1}$	$D^*/\text{Jones}$	LDR/dB	Response time	Effective wavelength range [nm]	Ref
$\text{MoS}_2/\text{Si}$	10.07	$4.53 \times 10^{10}$		78 $\mu\text{s}$	850	[38]
$\text{MoS}_2/\text{Si}$	300	$10^{13}$		3 $\mu\text{s}$	450–1050	[39]
$\text{WS}_2/\text{Si}$	4	$1.5 \times 10^{10}$	26	1.1 $\mu\text{s}$	400–850	[40]
$\text{WS}_2/\text{WTe}_2$	1325	$3.96 \times 10^{11}$	30		635	[41]
$\text{MoTe}_2/\text{InSe}$	15.4	$3.02 \times 10^{14}$	7.9	0.72 s	405–635	[42]
$\text{Bi}/\text{Si}$	8000	$1.9 \times 10^{10}$	19.8	3 $\mu\text{s}$	800	[43]
$\text{Te}/\text{Ge}$	523	$9.5 \times 10^{10}$		26 $\mu\text{s}$	400–980	[44]
$\text{Te}/\text{Si}$	6490	$7.79 \times 10^{12}$	18.9	26 ms	400–1100	[45]
$\text{Te NMs}/\text{Si}$	350	$9.6 \times 10^{11}$	45.5	70 $\mu\text{s}$	400–1550	This work

The LDRs in the table were calibrated by Equation (3).



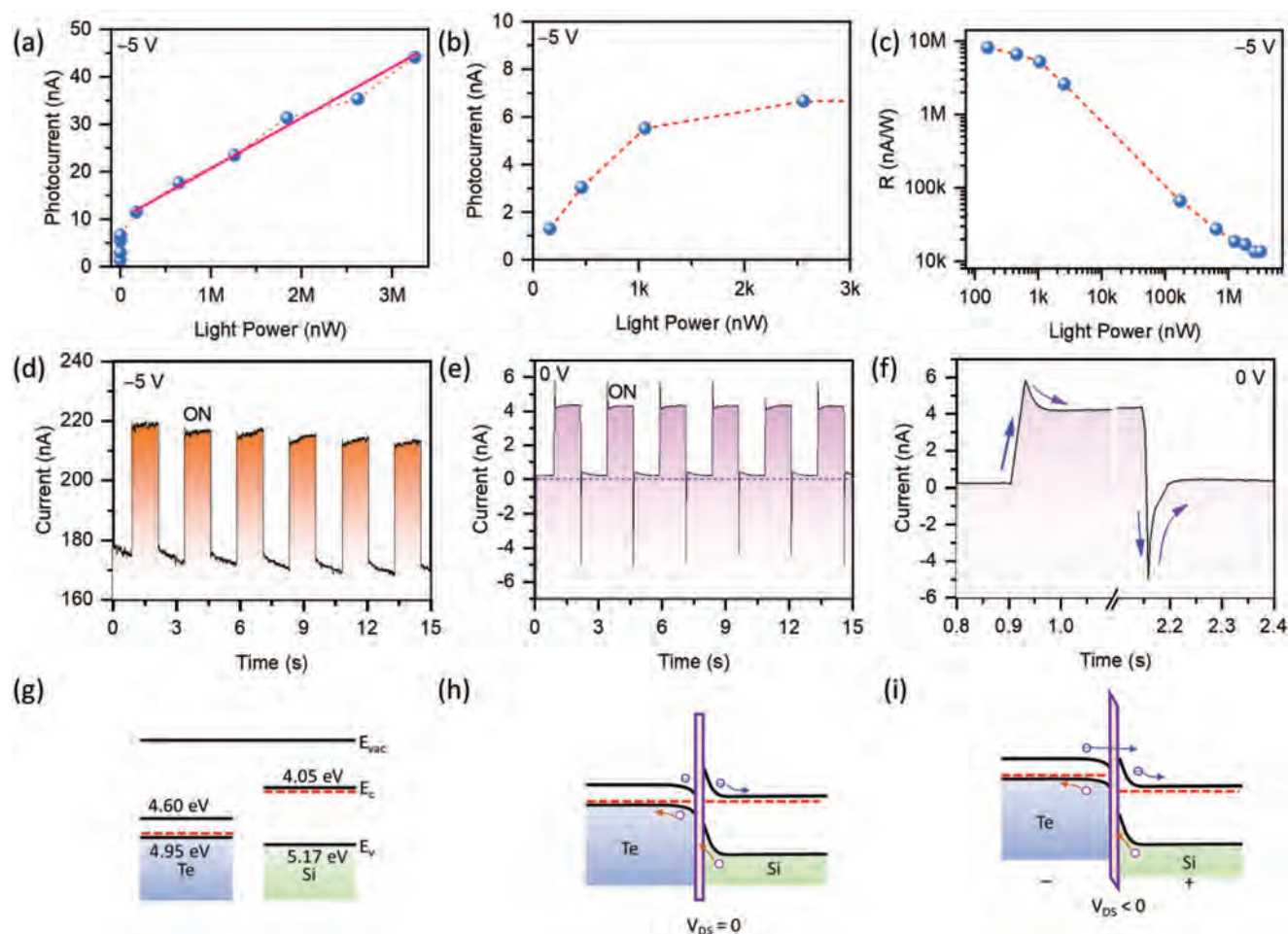


**Figure 5.** Photoresponse at 1550 nm and band alignment of the heterostructure. a) Photocurrent as a function of light power. b) Photocurrent as a function of light power with low light powers. c) Responsivity as a function of light power. d) Current-time curve under modulated light radiation with a bias voltage of  $-5$  V. e) Current-time curve under modulated light radiation with zero bias voltage. f) Magnified section of (e). The light power for (d–f) is 3.25 mW. g) Band alignment before contact. h) Band alignment after contact. i) Band alignment under reverse bias.

random size distribution of the Si pyramids, which leads to an uneven light-trapping effect. The photocurrent diminishes as the distance from the heterojunction region increases. For clarity on the variation trend, the photocurrent along the white dashed line in Figure 4e was extracted and presented in Figure 4f. The relationship between the photocurrent and distance can be modeled by an exponential decay curve with a decay length of  $14.7 \mu\text{m}$ . The exponential decay of the photocurrent indicates that the photoresponse away from the heterojunction is due to the diffusion of photogenerated carriers. Photogenerated holes in n-Si and photogenerated electrons in Te nanomesh away from the heterojunction region can diffuse into the heterojunction region and be collected, resulting in photocurrent. The decay length of the photocurrent is determined by both the diffusion length of photogenerated minority carriers in n-Si and p-Te nanomesh. Given that the decay length is significantly smaller than the junction area of the device, it is appropriate to consider the junction area as the photosensitive area without leading to substantial deviation from the true value.

Due to the narrow band gap of Te ( $\approx 0.35$  eV),<sup>[32]</sup> the heterostructure photodetector is expected to respond to infrared

light. We then conducted a measurement of the photoresponse to 1550 nm infrared light, as shown in Figure 5. The relationship between the photocurrent and light power is illustrated in Figure 5a. The detector demonstrates a linear response at high light power, while a sublinear relation is observed at low light power, as presented in Figure 5b. Consequently, the responsivity of the detector shows significant dependence on light power, as demonstrated in Figure 5c, reaching a maximum responsivity of  $8.1 \text{ mA W}^{-1}$  at a light power of  $0.16 \mu\text{W}$ . This behavior is also observed in the absence of bias voltage, as shown in Figure S8 (Supporting Information). The current-time curve under modulated light radiation is displayed in Figure 5d, demonstrating stable on-and-off states when the light is turned on and off. Similarly, the current-time curve with zero bias, as shown in Figure 5e, also displays stable current on and off states. Notably, spikes in current are observed when light is turned on or off. A magnified view of the spikes is presented in Figure 5f. The detector exhibits a rapid increase when light is turned on, followed by a slow decay. Conversely, when the light is turned off, the detector shows a sharp decrease, even dropping to a negative value, followed by a slow rise to the stable dark current.

This unique behavior stems from the specific band alignment between Te nanomesh and Si, which will be discussed in the following section. The appearance spikes, which exhibit different signs when the light is turned on and off, could potentially find applications in the event-driven vision sensors.<sup>[46]</sup>

The band alignment before contact is depicted in Figure 5g, revealing a type I band alignment between Te and Si.<sup>[47]</sup> Upon contact, electrons diffuse from Si to Te, and holes diffuse from Te to Si due to the difference in the work functions of the two materials. Consequently, band bending occurs near the interface, culminating in a unified Fermi level for the heterojunction system, as illustrated in Figure 5h. The band bending gives rise to an internal electrical field directed from Si to Te. A vdW barrier arises near the interface due to Te's quasi-1D vdW crystal structure, resulting in a vdW gap formation between Te and Si after contact.<sup>[48]</sup> Additionally, an energy valley forms on the conduction band of Te near the interface owing to the type I band alignment. First, the photon energy is larger than the band gap of Si is considered. Upon light radiation, photogenerated electron-hole pairs can be separated and collected by the internal electrical field, leading to the photovoltaic effect. However, the transport of the photogenerated electrons in Te is impeded by the vdW gap and the energy valley. Likewise, the transport of holes from Si to Te is partially obstructed by the vdW gap, resulting in the trap of some photogenerated holes in Si at the vdW gap. Consequently, the collection efficiency of the photogenerated carriers is diminished, yielding a weak photovoltaic effect at zero bias, consistent with experimental results. Most photogenerated carriers are generated on the Si side when the incident light photon energy exceeds the band gap of Si, which is attributable to the Te layer's thin thickness and mesh-like structure. The photogenerated electron-hole pairs are separated by the internal electrical field. Electrons drift away from the depletion region and enter the Si side, while holes must traverse the vdW gap and be collected at the Te side. The vdW gap impedes the transport of holes to the Te side, trapping some photogenerated holes. At low light powers, the number of trapped holes at the vdW gap is small, and only a limited quantity of electrons recombines with holes, resulting in the observed linear relationship shown in Figure 3g. Nevertheless, the enhanced number of photogenerated carriers increases the recombination rate under high light power, leading to a sublinear relationship between photocurrent and light power. When a reverse bias voltage is applied, the Fermi level of Si compared with Te is lowered, as shown in Figure 5i. The band offset at the conduction band is diminished while the band offset at the valence band is increased due to a finite voltage drop on the vdW gap. Moreover, the band bending intensifies owing to the enhanced electrical field in the depletion region. Consequently, the trapped photogenerated holes near the vdW gap can be transported to the Te side by means of tunneling. The collection efficiency is enhanced and reaches a maximum when the bias voltage is sufficiently high. A further increase of the reverse bias voltage does not enhance the collection efficiency, resulting in the saturation of the photocurrent.

When the photon energy is lower than the band gap of Si, the majority of photogenerated carriers are produced in the Te nanomesh. The trapping capability of the electron valley in the Te side at the interface is much stronger than the vdW gap. Consequently, the photogenerated electrons cannot escape from the

valley under zero bias. The recombination rate of photogenerated carriers is directly related to the trapped electrons in the valley, resulting in the observed sublinear relation at low light powers, as shown in Figure S5 (Supporting Information). Once the valley becomes fully occupied by electrons, the recombination rate stabilizes, yielding a linear relationship. Even under reverse bias, the valley can still trap photogenerated electrons, resulting in similar behavior to that observed under zero bias, as shown in Figure 5a,b.

The electron trapping effect by the energy valley also contributes to the observation of current spikes when light is turned on and off, as shown in Figure 5e. In conjunction with the pn junction structure, the electron energy valley functions as a capacitor. When light is turned on, the photogenerated carriers are separated by the built-in electrical field at the junction and are subsequently collected at the electrodes. This process results in the rapid rise of the photocurrent. Additionally, a portion of the photogenerated electrons in Te is injected into the valley. To maintain the charge balance of the junction, photogenerated holes in Si are attracted to the interface, thus simulating the charging of a capacitor. Consequently, the positive spike is observed, similar to the charging current curve of a capacitor. When light is turned off, the trapped electrons are released, akin to the discharging of a capacitor, resulting in the observation of a negative spike. The disappearance of the spikes under reverse bias is attributed to the reduced electron valley barrier. Based on the mechanism, the occurrence of spikes is not limited to 1550 nm but rather observed whenever the photon energy surpasses the bandgap of Te nanomesh. In fact, spikes were also observed when visible light was used as a light source and a source-measurement unit with a shorter integration time, as shown in Figure S9 (Supporting Information). To mitigate the impact of these peaks, the device should be operated either in a reverse bias mode or in a low-frequency mode with a low-frequency pass filter.

Due to the broadband and decent photoresponse of the photodetector, we performed further studies on visible light and infrared imaging using the Te nanomesh/black-Si heterostructure device as the imaging pixel. The imaging measurement system is schematically depicted in Figure 6a, where a shadow mask was securely placed on a 2D translation stage, and the heterostructure photodetector served as the sensing pixel. Under light radiation, the photodetector captures the transmitted light point-by-point and outputs the photocurrent matrix. The position-dependent photocurrents with different light wavelengths are shown in Figure 6b–e, and the letters “UESTC” in the mask can be clearly reproduced. It is noted that the recorded image at 1550 nm exhibits significant noise, which can be attributed to the low responsivity of the photodetector at 1550 nm and the large light spot of the 1550 nm light on the mask. Nonetheless, the imaging results indicate that the heterostructure photodetector demonstrates ultra-broadband imaging capability.

### 3. Conclusion

In conclusion, we have successfully fabricated a Te nanomesh/black-Si vdW pn heterostructure photodetector. The heterostructure exhibits the distinctive rectification behavior with a rectification ratio of  $2.2 \times 10^4$ . Comprehensive photoresponse measurements demonstrate the commendable



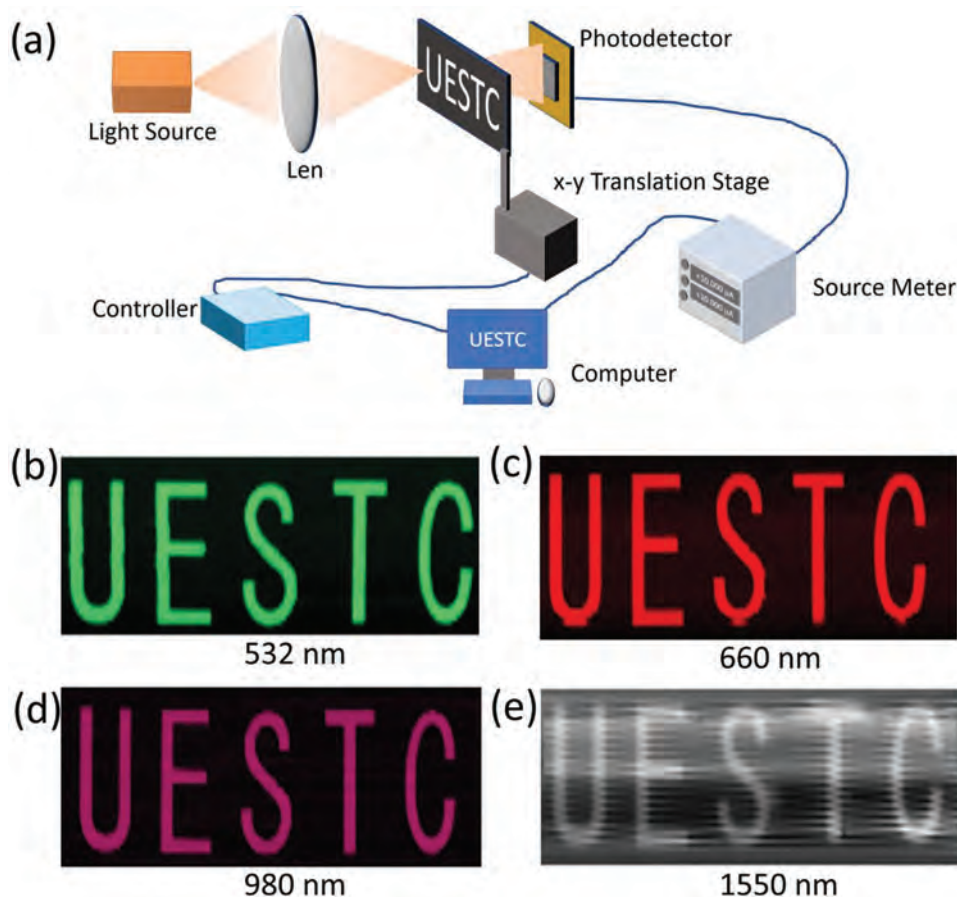


**Figure 6.** Imaging demonstration of the heterostructure photodetector. a) Schematic of the broadband imaging system. b–e) Imaging results of the shadow with hollow letters of “UESTC” recorded under light sources with different wavelengths. (b) 532 nm. (c) 660 nm. (d) 980 nm. (e) 1550 nm. The bias voltage is  $-5$  V for all the measurements.

performance of the heterostructure device, including a high responsivity of  $350 \text{ mA W}^{-1}$ , an extensive linear dynamic range of 45.5 dB, a high specific detectivity of  $9.6 \times 10^{11}$  Jones, and a wide spectral response ranging from 400 to 1550 nm. Moreover, the heterostructure device exhibits remarkable response speeds, with a rise time and a decay time of 70 and 140  $\mu\text{s}$ , respectively. The exceptional performance can be attributed to the presence of a strong internal built-in electrical field at the hetero-interface and the enhanced light absorption in black-Si through the light trapping effect. These outstanding photoresponse properties make the heterostructure device highly suitable for application as a multiwavelength single-pixel imager, enabling the collection of mask patterns under light radiation with varying wavelengths. Our work introduces a novel approach for fabricating mixed-dimensional vdW heterostructures, holding great promise for the advancement of next-generation optoelectronics.

#### 4. Experimental Section

**Preparation of Black-Si:** The  $\text{SiO}_2$  (285 nm)/n-Si (1–10  $\Omega\cdot\text{cm}$ ) substrate was employed for the preparation of black-Si. Utilizing a maskless photolithography technique with a DL10 (Zytools) system, a defined win-

dow with a size of  $5 \times 5 \text{ mm}^2$  was created. Subsequently, an ion etching technique was employed to selectively remove the  $\text{SiO}_2$  layer, exposing the underlying Si substrate. In the ion etching process,  $\text{CF}_4$  (200 sccm) and Ar (100 sccm) were used as process gases, the etching power was set to 100 W, and the etching time was 360 s. The transformation of the Si substrate into black-Si was achieved through an alkaline wet etching method. The alkaline solution was prepared by dissolving KOH (2.98 g) in a mixed solution of isopropanol (20 mL) and deionized water (80 mL). The etching process was carried out at a temperature of  $95^\circ\text{C}$  for a duration of 40 min. The thickness of black-Si is 2–5  $\mu\text{m}$ .

**Fabrication of Te Nanomesh/Black-Si Heterostructure:** Prior to the deposition of the Te nanomesh, a Ti (5 nm)/Au (50 nm) layer was deposited on the  $\text{SiO}_2$  layer surrounding the black-Si window using an e-beam evaporation method. This layer functioned as the top electrode. The deposition process for the Te nanomesh onto the black-Si substrate was carried out in a two-zone horizontal tube furnace. The prepared black-Si was positioned within the low-temperature heating zone ( $100^\circ\text{C}$ ), while 1 g of Te powder (99.99%) was placed inside the high-temperature heating zone ( $450^\circ\text{C}$ ). To remove oxygen from the system, the tube was purged with argon gas (200–300 sccm) for 30 min prior to heating. Subsequently, argon gas with a flow rate of 15 sccm was introduced into the tube furnace, and the heating process was initiated. After an 8-h deposition period, a dense Te nanomesh was formed on the surface of the black-Si substrate.

**Characterization:** The Raman spectra of Te nanomesh were measured using a Raman spectrometer (SR-5001-A-R, Andor) with a 532 nm laser as the excitation source. SEM images were obtained using a scanning elec-

tron microscope (VEGA3 SBH, TESCAN). AFM images were obtained using an atomic force microscope (NX10, Park). TEM and HRTEM images were obtained using a transmission electron microscope (JEOL 2100F).

**Electrical and Photodetection Performance Measurements:** The electrical properties were measured in a probe station (LN-4H-06, ZepTools) with a Keysight B1500A semiconductor analyzer. The photodetection performance of the devices was measured in an optoelectronic measurement system (ScanPro Advance, MetaTest) with a Keithley 2636B source measurement meter. The position-dependent current in the imaging system was recorded by synchronizing an Agilent B2902A source-measurement meter with a motorized 2D translational stage through a data acquisition card (Myrio-1900, NI). The imaging system utilized a 532 nm laser, a 660 nm light-emitting diode, a 980 nm light-emitting diode, and a 1550 nm laser as the light sources. The spot size for 532, 660, and 980 nm lights is  $\approx 0.2$  mm, whereas the spot size for 1550 nm light was  $\approx 1$  mm. The mask dimensions were  $4\text{ cm} \times 1\text{ cm}$ , with the smallest hollow part measuring 1 mm (Figure S10, Supporting Information).

## Supporting Information

Supporting Information is available from the Wiley Online Library or from the author.

## Acknowledgements

This work was supported by the National Natural Science Foundation of China (Grant Nos. 61975024 and 62074024), the Sichuan Science and Technology Program (Grant Nos. 2023YFH0090 and 2023NSFSC0365), and the Natural Science Foundation of Sichuan Province (Grant No. 2022NSFSC0042).

## Conflict of Interest

The authors declare no conflict of interest.

## Data Availability Statement

The data that support the findings of this study are available from the corresponding author upon reasonable request.

## Keywords

black-Si, heterostructure, photodetectors, Te nanomesh, van der Waals

Received: January 7, 2024

Revised: April 1, 2024

Published online: April 18, 2024

- [1] Z. Zhao, J. Liu, Y. Liu, N. Zhu, *J. Semicond.* **2017**, *38*, 121001.
- [2] S. Y. Cho, N. M. Jokerst, *Appl. Phys. Lett.* **2007**, *90*, 101105.
- [3] A. Rogalski, *Opto-Electron. Rev.* **2012**, *20*, 279.
- [4] J. Wang, X. W. Xu, S. Xiao, Y. Li, W. Qian, J. Yu, K. Zhang, S. H. Yang, *Adv. Opt. Mater.* **2021**, *9*, 2100517.
- [5] J. Kaniewski, J. Piotrowski, *Opto-Electron. Rev.* **2004**, *12*, 139.
- [6] A. Rogalski, P. Martyniuk, M. Kopytko, *Appl. Phys. Rev.* **2017**, *4*, 031304.
- [7] A. D. Stiff-Roberts, *J. Nanophotonics* **2009**, *3*, 031607.

- [8] A. Rogalski, *Infrared Phys. Technol.* **2002**, *43*, 187.
- [9] C. Y. Lan, C. Li, J. C. Ho, Y. Liu, *Adv. Electron. Mater.* **2021**, *7*, 2000688.
- [10] P. Ares, K. S. Novoselov, *Nano Mater. Sci.* **2022**, *4*, 3.
- [11] C. Y. Lan, Z. Shi, R. Cao, C. Li, H. Zhang, *Nanoscale* **2020**, *12*, 11784.
- [12] L. H. Zeng, D. Wu, J. S. Jie, X. Y. Ren, X. Hu, S. P. Lau, Y. Chai, Y. H. Tsang, *Adv. Mater.* **2020**, *32*, 2004412.
- [13] L. H. Zeng, W. Han, X. Y. Ren, X. Li, D. Wu, S. J. Liu, H. Wang, S. P. Lau, Y. H. Tsang, C. X. Shan, J. S. Jie, *Nano Lett.* **2023**, *23*, 8241.
- [14] L. H. Zeng, S. H. Lin, Z. J. Li, Z. X. Zhang, T. F. Zhang, C. Xie, C. H. Mak, Y. Chai, S. P. Lau, L. B. Luo, Y. H. Tsang, *Adv. Funct. Mater.* **2018**, *28*, 1705970.
- [15] L. H. Zeng, W. Han, S. E. Wu, D. Wu, S. P. Lau, Y. H. Tsang, *IEEE Trans. Electron Devices* **2022**, *69*, 6212.
- [16] D. Wu, C. G. Guo, L. H. Zeng, X. Y. Ren, Z. F. Shi, L. Wen, Q. Chen, M. Zhang, X. J. Li, C. X. Shan, J. S. Jie, *Light Sci Appl* **2023**, *12*, 5.
- [17] D. Wu, J. W. Guo, J. Du, C. X. Xia, L. H. Zeng, Y. Z. Tian, Z. F. Shi, Y. T. Tian, X. J. Li, Y. H. Tsang, J. S. Jie, *ACS Nano* **2019**, *13*, 9907.
- [18] D. Wu, J. W. Guo, C. Q. Wang, X. Y. Ren, Y. S. Chen, P. Lin, L. H. Zeng, Z. F. Shi, X. J. Li, C. X. Shan, J. S. Jie, *ACS Nano* **2021**, *15*, 10119.
- [19] L. H. Zeng, D. Wu, S. H. Lin, C. Xie, H. Y. Yuan, W. Lu, S. P. Lau, Y. Chai, L. B. Luo, Z. J. Li, Y. H. Tsang, *Adv. Funct. Mater.* **2019**, *29*, 1806878.
- [20] L. H. Zeng, Q. M. Chen, Z. X. Zhang, D. Wu, H. Y. Yuan, Y. Y. Li, W. Qarony, S. P. Lau, L. B. Luo, Y. H. Tsang, *Adv. Sci.* **2019**, *6*, 1901134.
- [21] D. Wu, M. M. Xu, L. H. Zeng, Z. F. Shi, Y. Z. Tian, X. J. Li, C. X. Shan, J. S. Jie, *ACS Nano* **2022**, *16*, 5545.
- [22] X. C. Yu, P. Yu, D. Wu, B. Singh, Q. S. Zeng, H. Lin, W. Zhou, J. H. Lin, K. Suenaga, Z. Liu, Q. J. Wang, *Nat. Commun.* **2018**, *9*, 1545.
- [23] Y. Y. Wei, C. Y. Lan, S. R. Zhou, C. Li, *Appl. Sci.-Basel* **2023**, *13*, 11037.
- [24] Z. J. Lu, Y. Xu, Y. Q. Yu, K. W. Xu, J. Mao, G. B. Xu, Y. M. Ma, D. Wu, J. S. Jie, *Adv. Funct. Mater.* **2020**, *30*, 1907951.
- [25] F. X. Liang, X. Y. Zhao, J. J. Jiang, J. G. Hu, W. Q. Xie, J. Lv, Z. X. Zhang, D. Wu, L. B. Luo, *Small* **2019**, *15*, 1903831.
- [26] D. Wu, C. Jia, F. H. Shi, L. H. Zeng, P. Lin, L. Dong, Z. F. Shi, Y. T. Tian, X. J. Li, J. S. Jie, *J. Mater. Chem. A* **2020**, *8*, 3632.
- [27] S. R. Zhou, H. D. Fan, S. F. Wen, R. Zhang, Y. Yin, C. Y. Lan, C. Li, Y. Liu, *Adv. Opt. Mater.* **2024**, *12*, 2301982.
- [28] Z. H. Yan, H. Yang, Z. Yang, C. G. Ji, G. Y. Zhang, Y. S. Tu, G. Y. Du, S. H. Cai, S. H. Lin, *Small* **2022**, *18*, 2200016.
- [29] Z. He, Y. Yang, J. W. Liu, S. H. Yu, *Chem. Soc. Rev.* **2017**, *46*, 2732.
- [30] M. Amani, C. L. Tan, G. Zhang, C. S. Zhao, J. Bullock, X. H. Song, H. Kim, V. R. Shrestha, Y. Gao, K. B. Crozier, M. Scott, A. Javey, *ACS Nano* **2018**, *12*, 7253.
- [31] M. Peng, R. Z. Xie, Z. Wang, P. Wang, F. Wang, H. N. Ge, Y. Wang, F. Zhong, P. S. Wu, J. F. Ye, Q. Li, L. L. Zhang, X. Ge, Y. Ye, Y. C. Lei, W. Jiang, Z. G. Hu, F. Wu, X. H. Zhou, J. S. Miao, J. L. Wang, H. G. Yan, C. X. Shan, J. N. Dai, C. Q. Chen, X. S. Chen, W. Lu, W. D. Hu, *Sci. Adv.* **2021**, *7*, eabf7358.
- [32] J. Treusch, R. Sandrock, *Phys. Status. Solidi.* **1966**, *16*, 487.
- [33] Y. Meng, X. C. Li, X. L. Kang, W. P. Li, W. Wang, Z. X. Lai, W. J. Wang, Q. Quan, X. M. Bu, S. Yip, P. S. Xie, D. Chen, D. J. Li, F. Wang, C. F. Yeung, C. Y. Lan, C. T. Liu, L. F. Shen, Y. Lu, F. R. Chen, C. Y. Wong, J. C. Ho, *Nat. Commun.* **2023**, *14*, 2431.
- [34] H. C. Casey, J. Muth, S. Krishnankutty, J. M. Zavada, *Appl. Phys. Lett.* **1996**, *68*, 2867.
- [35] P. Perlin, M. Osinski, P. G. Eliseev, V. A. Smagley, J. Mu, M. Banas, P. Sartori, *Appl. Phys. Lett.* **1996**, *69*, 1680.
- [36] J. P. Xu, X. G. Luo, X. Lin, X. Zhang, F. Liu, Y. T. Yan, S. Q. Hu, M. W. Zhang, N. N. Han, X. T. Gan, Y. C. Cheng, W. Huang, *Adv. Funct. Mater.* **2024**, *34*, 2310811.
- [37] X. H. An, F. Z. Liu, Y. J. Jung, S. Kar, *Nano Lett.* **2013**, *13*, 909.
- [38] J. M. Choi, H. Y. Jang, A. R. Kim, J. D. Kwon, B. Cho, M. H. Park, Y. Kim, *Nanoscale* **2021**, *13*, 672.
- [39] L. Wang, J. S. Jie, Z. B. Shao, Q. Zhang, X. H. Zhang, Y. M. Wang, Z. Sun, S. T. Lee, *Adv. Funct. Mater.* **2015**, *25*, 2910.

- [40] H. S. Kim, M. Patel, J. Kim, M. S. Jeong, *ACS Appl. Mater. Interfaces* **2018**, *10*, 3964.
- [41] J. Y. Ma, J. A. Wang, Q. Chen, S. D. Chen, M. M. Yang, Y. M. Sun, Z. Q. Zheng, N. J. Huo, Y. Yan, J. B. Li, W. Gao, *Adv. Electron. Mater.* **2024**, *10*, 2300672.
- [42] Y. M. Sun, W. Gao, X. P. Li, C. X. Xia, H. Y. Chen, L. Zhang, D. X. Luo, W. J. Fan, N. J. Huo, J. B. Li, *J. Mater. Chem. C* **2021**, *9*, 10372.
- [43] Z. Y. Dang, W. H. Wang, J. Y. Chen, E. S. Walker, S. R. Bank, D. Akinwande, Z. H. Ni, L. Tao, *2D Mater.* **2021**, *8*, 035002.
- [44] B. N. Zheng, Z. H. Wu, F. Guo, R. Ding, J. F. Mao, M. H. Xie, S. P. Lau, J. H. Hao, *Adv. Opt. Mater.* **2021**, *9*, 2101052.
- [45] T. Zheng, M. M. Yang, Y. M. Sun, L. X. Han, Y. Pan, Q. X. Zhao, Z. Q. Zheng, N. J. Huo, W. Gao, J. B. Li, *J. Mater. Chem. C* **2022**, *10*, 7283.
- [46] Y. Zhou, J. W. Fu, Z. R. Chen, F. W. Zhuge, Y. S. Wang, J. M. Yan, S. J. Ma, L. Xu, H. M. Yuan, M. S. Chan, X. S. Miao, Y. H. He, Y. Chai, *Nat. Electron.* **2023**, 870.
- [47] J. T. Lu, L. J. Zhang, C. R. Ma, W. J. Huang, Q. J. Ye, H. X. Yi, Z. Q. Zheng, G. W. Yang, C. A. Liu, J. D. Yao, *Nanoscale* **2022**, *14*, 6228.
- [48] A. Allain, J. H. Kang, K. Banerjee, A. Kis, *Nat. Mater.* **2015**, *14*, 1195.